NANO LETTERS

pubs.acs.org/NanoLett Letter

Emergent Magnetism with Continuous Control in the Ultrahigh-Conductivity Layered Oxide $PdCoO_2$

Matthew Brahlek,* Alessandro R. Mazza, Abdulgani Annaberdiyev, Michael Chilcote, Gaurab Rimal, Gábor B. Halász, Anh Pham, Yun-Yi Pai, Jaron T. Krogel, Jason Lapano, Benjamin J. Lawrie, Gyula Eres, Jessica McChesney, Thomas Prokscha, Andreas Suter, Seongshik Oh, John W. Freeland, Yue Cao, Jason S. Gardner, Zaher Salman, Robert G. Moore, Panchapakesan Ganesh,* and T. Zac Ward

Cite This: https://doi.org/10.1021/acs.nanolett.3c01065 Read Online

ACCESS | Metrics & More | Article Recommendations | * Supporting Information

ABSTRACT: The current challenge to realizing continuously tunable magnetism lies in our inability to systematically change properties, such as valence, spin, and orbital degrees of freedom, as well as crystallographic geometry. Here, we demonstrate that ferromagnetism can be externally turned on with the application of low-energy helium implantation and can be subsequently erased and returned to the pristine state via annealing. This high level of continuous control is made possible by targeting magnetic metastability in the ultrahigh-conductivity, nonmagnetic layered oxide $PdCoO_2$ where local lattice distortions generated by helium implantation induce the emergence of a net moment on the surrounding transition metal octahedral sites. These highly localized moments communicate through the itinerant metal states, which trigger the onset of percolated long-range ferromagnetism. The ability to continuously tune competing interactions enables tailoring precise magnetic and magnetotransport responses in an ultrahigh-conductivity film and will be critical to applications across spintronics.

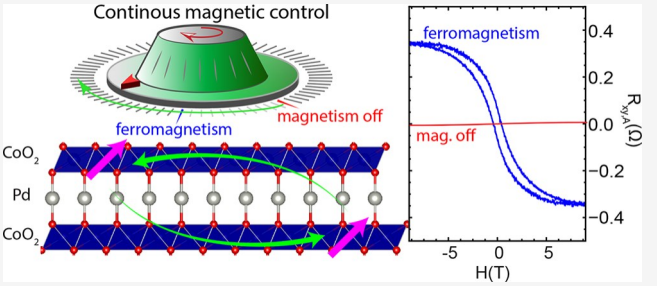

KEYWORDS: *delafossite, molecular beam epitaxy, magnetism, implantation, anomalous Hall effect, spintronics*

Designing novel materials systems with flexible control over magnetic phase and properties is central to enabling new devices with superior energy eficiency and increased computational power.[1,2] Specifically, magnetic metals are critical to the development of next-generation spintronic devices based on, for example, spin-transfer torques. Yet, tailoring magnetic properties in traditional systems has been limited to controlling interfaces or alloying.[3] Tuning magnetism in a continuous way is challenging because the electronic and magnetic character are linked through the exchange interaction to the specific intrinsic properties within a material, including their charge states, net moments, and bonding environments. Targeted control of these interactions has been achieved via external voltage control,[4] thickness scaling,[5−7] and strain in freestanding films[8] in systems that are already magnetic, yet new routes are necessary for future applications where magnetism can be induced and controlled in a continuous and metastable way. Toward this, transition metal oxides possess strongly correlated spin, orbital, and charge degrees of freedom, all of which are necessary for materials tunablility,[9] but in practice, magnetic metal oxides are rare and usually exhibit relatively high resistivities.[10,11] Notable exceptions are the 2-dimensional (2D) ABO_2 metallic delafossites, shown in Figure 1a, which represent a unique material system that has garnered significant recent attention[12,13] due to a myriad of unusual fundamental properties[14−17] as well as novel functional responses.[18−21] For $PdCoO_2$, $PtCoO_2$ and $PdCrO_2$ this class of oxides provides a highly anisotropic layered crystal structure in which the *A*-site and *B*-site sublattice layers have extraordinarily different properties.[12] Specifically, the Pd/Pt layers give rise to extremely high conductivity,[22] whereas the states in the Co/Cr layers are highly localized and insulating.[23,24] The sole magnetic delafossite, Cr-based $PdCrO_2$, exhibits a stable and nontunable antiferromagnetic state.[25] On the other hand, Co-based $PdCoO_2$ is a nonmagnetic, Pauli paramagnet but likely resides near a magnetic metastability. Here, the octahedrally coordinated Co^{3+}, shown in Figure 1b, is in a low-spin state that is known to be in proximity to the intermediate (M = 2 μ_B/Co) and high (M = 4 μ_B/Co) spin states accessible through

Received: March 20, 2023
Revised: July 6, 2023

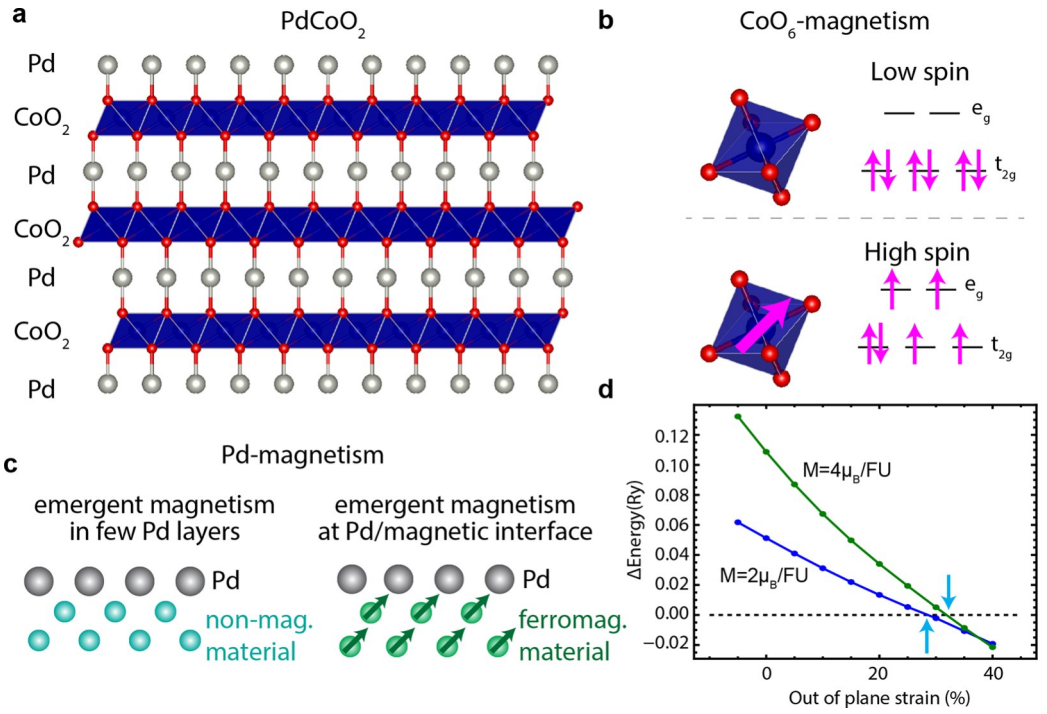

Figure 1. Illustration of magnetic metastability of $PdCoO_2$ (a) Schematic of the delafossite structure composed of alternating Pd and CoO_2 layers. (b, c) Magnetic metastability in $PdCoO_2$ due to the close proximity of the nonmagnetic ($M = 0\ \mu_B$/Co low-spin) and a magnetic state ($M = 4\ \mu_B$/Co high-spin, shown) known in octahedral coordinated Co^{3+} and (c) the large density of states of bulk Pd, which is known to become magnetic in the monolayer limit (left), and when interfaced with a ferromagnetic material (right), represented by green arrows. (d) Calculated energy difference among the strained magnetic cells with intermediate ($M = 2\ \mu_B$/formula unit (FU), blue) and high-spin ($M = 4\ \mu_B$/FU, green) relative to the unstrained nonmagnetic states, which shows a crossover with a large out-of-plane strain (indicated by the blue arrows).

strain and charge doping.[26] Similarly, bulk Pd is also well-known to be close to a Stoner instability due to the high density of states at the Fermi level (E_F),[27] which can become magnetic when made atomically thin[28] or at an interface with a magnet,[29] as shown in Figure 1c. Moreover, the strong spin–orbit coupling associated with metal layers of Pd can give rise to important functional properties, such as magnetic anisotropy, spin torque, novel domain wall structures, and topological spin textures.[1] While attempts at stabilizing ferromagnetism using traditional magnetic doping on the Co site have not been successful,[30] hints of surface magnetism have been observed in cleaved bulk crystals[31,32] and in thin films.[33] A systematic uniform modification of the bulklike magnetic responses in $PdCoO_2$ has not been predicted or demonstrated experimentally, which highlights that new routes are needed to induce and control this fundamental property. These aspects together make $PdCoO_2$ an extremely promising candidate for tailoring magnetism in a high-conductivity, low-dimensional/nanostructured platform.

Here, we reveal a route to induce magnetism with a high level of continuous control in highly conducting $PdCoO_2$ thin films. Experimentally, it is shown that the helium implantation in $PdCoO_2$ can systematically cause strain along the out-of-plane direction while fully retaining the structural and chemical character. This is effectively found to tune from the nonmagnetic ground state of the pristine structure to a paramagnetic state with net moments and finally to a ferromagnetic ground state that exhibits long-range order and clear hysteresis with onset near 150 K. These results closely match models in which uniaxial out-of-plane strain pushes the Co sites into a spin-polarized state near local lattice distortions; the induced moments on the Co site then magnetize the itinerant Pd states to stabilize long-range ferromagnetic order. Magnetotransport is used to map the evolution of the anomalous Hall effect (AHE), which clearly demonstrates a strain-induced crossover in scattering mechanisms. Finally, the magnetic state is found to be fully reversible via high temperature annealing, which resets the system to the pristine state. These observations give insight into how magnetism emerges in a low-dimensional system that combines both itinerant and localized physics, as well as being a highly tunable platform for creating nanoscale magnetic devices with previously inaccessibly high electrical conductivity.

To understand how strain can be used to induce magnetism in $PdCoO_2$, first-principles calculations were performed as a function of distortion to the unit cell (Supporting Information, Section I). As previous reports have shown, helium implantation can be used to generate an out-of-plane expansion of the lattice while the in-plane lattice remains heteroepitaxially locked and unchanged,[34−37] so calculations were performed by applying an out-of-plane expansion to the unit cell. Because $PdCoO_2$ shows itinerate and localized physics, density functional theory + U calculations[38] informed by quantum Monte Carlo (QMC)[39,40] were performed to minimize ambiguities in the choice of the U parameter.[41] Figure 1d shows the energy difference for the distorted unit cell with $M = 2\ \mu_B$ per formula unit (FU; the spin is not confined to the Co, see the Supporting Information; intermediate spin) and $M = 4\ \mu_B$/FU (high spin) relative to the undistorted, nonmagnetic unit cell versus out-of-plane strain. With increasing strain, there is a crossover into a magnetic phase near 30%, as marked by the blue arrows. Moreover, there is a large mixing of the magnetic Co into the

https://doi.org/10.1021/acs.nanolett.3c01065
Nano Lett. XXXX, XXX, XXX−XXX

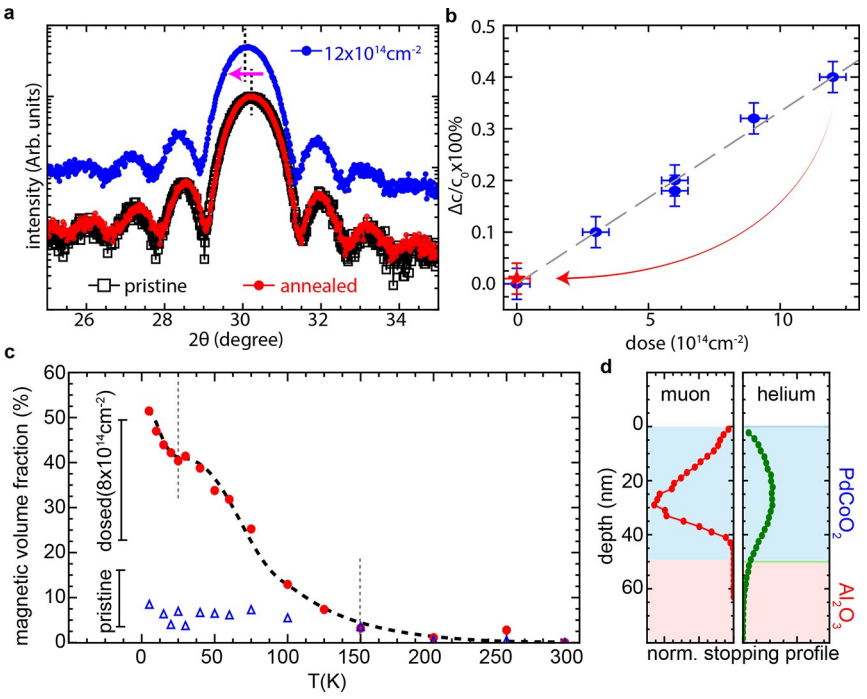

Figure 2. Implantation-induced strain and emergent ferromagnetism. (a) $2\vartheta-\vartheta$ scans about the 006 $PdCoO_2$ reflection for a pristine sample, an implanted sample, and a sample reset with a post implantation anneal. (b) Systematic expansion of the out-of-plane lattice parameter, $\Delta c/c_0 \times 100\%$, for an implanted series (blue circles) and a sample that was reset with a post implantation anneal (red star). (c) Temperature dependence of the magnetic volume fraction for an implanted sample and pristine sample measured with low-energy muon spin rotation. (d) Simulated normalized muon implantation profile (left panel) in comparison to the helium implantation profile (right panel).

density of states at the Fermi level (see Figure S5). This mixing of magnetic Co orbital character into the itinerant states generates a large hybridization between the Pd and Co electrons and is central to $PdCoO_2$ becoming magnetic. As such, novel approaches that are capable of creating and inducing magnetism in the delafossites are needed because progress toward percent-level epitaxial strain[13,42−44] and magnetic doping control in the delafossites[30] have been challenging. Metastable helium implantation is ideal to achieve very large distortions[34−36] that can locally reach the large, 30% strain that is necessary to drive $PdCoO_2$ into a magnetic state.

To test if distortions of the unit cell produce magnetism, detailed structural and electronic characterizations were performed as a function of helium dose on a series of molecular beam epitaxy grown thin films (thickness ≈ 10 nm; see ref 44 and Supporting Information Section IIA for growth and implantation details). Figure 2a shows X-ray diffraction $2\vartheta-\vartheta$ scans for the 006 reflection for pristine and highly dosed $PdCoO_2$ samples. Here, implantation rigidly shifts the peak to a lower 2ϑ, which corresponds to a coherent out-of-plane expansion. The change in the out-of-plane lattice parameter c, shown by $\Delta c/c \times 100\%$ in Figure 2b, is linear with dose and gives a maximum average strain of ⍰0.5% at a dose of 12×10^{14} cm^{-2}. Although the net or average strain is much less than that predicted by theory (⍰30%), there are likely regions of large strain surrounding an implanted helium atom, which we show later produces local moments. Moreover, the overall peak shape is unchanged, indicating that the dosing is homogeneous, and structural integrity is maintained. In a wide range $2\vartheta-\vartheta$ scan (Figure.S8), no additional peaks arise, which indicates that there is no damage to the film; for example, no Pd, Co, or PdCo peaks are observed.[19,20] Second, the small Laue oscillations about the main peak indicate that the films are nearly atomically flat, which, importantly, is not changed during implantation. This indicates that the surfaces are not damaged nor is the top layer sputtered away, thereby thinning the sample. This result is corroborated by the X-ray reflectivity measurements shown in Figure S9 and X-ray photoemission spectroscopy shown in Figure S10.

We highlight that the implantation process can be fully reset via annealing: Figure 2a shows a $2\vartheta-\vartheta$ scan for a $PdCoO_2$ film that was implanted and then annealed at 750 °C in air (red symbols), which is overlaid on the pristine data. The peak position shows that the c-axis lattice parameter exactly returns to the pristine state (red stars). Additionally, the peak character and Laue oscillations demonstrate that there is no change in the crystalline thickness or lattice quality that would occur if surface sputtering or bulk amorphousizing were present. Throughout these experiments, we saw no sign of damage or sample degradation across multiple implant/anneal steps. In contrast to previous studies,[45−47] this confirms that all effects induced by helium implantation are both stable to thermal processing as well as fully reversible.

To show that changes to lattice volume induces magnetism, low-energy muon spin rotation (μSR) measurements were performed, which is an extremely sensitive and direct probe of the depth-resolved magnetic profile in thin films (see refs 48 and 49 as well as Supporting Information Sections IID and IIIB). The magnetic volume fraction (MVF), extracted from fitting the muon decay profile, is shown for muon implantation energy of 6 keV for the dosed film as well as a pristine film. Here, a nonzero MVF indicates that magnetism can be created and stabilized using implantation, as shown in Figure 2c for a film dosed at 8×10^{14} cm^{-2} (circles). For this incident energy the muons probe deep into the bulk of the film, as shown in Figure 2d for the implantation distribution calculated using

https://doi.org/10.1021/acs.nanolett.3c01065
Nano Lett. XXXX, XXX, XXX−XXX

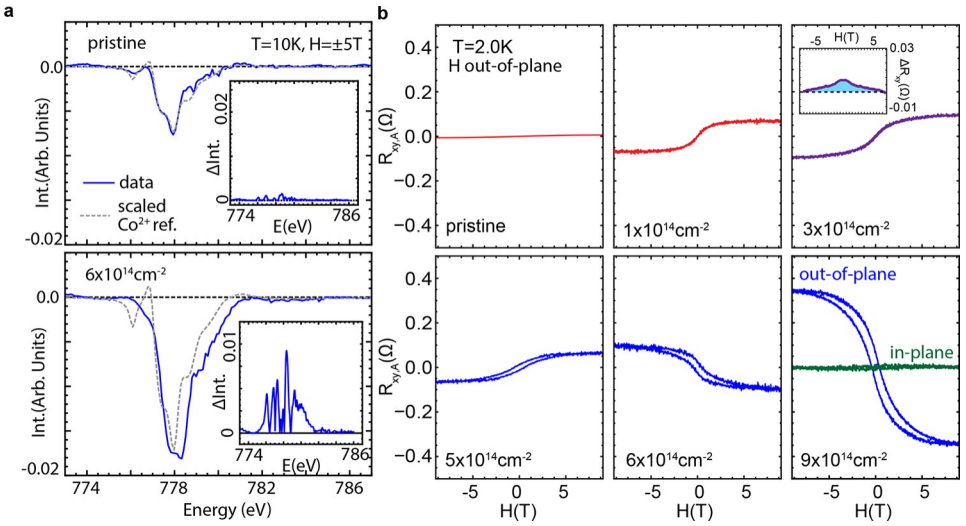

Figure 3. Continuously controlled magnetism and anomalous Hall effect. (a) XMCD spectra for a pristine (top) and implanted (bottom) sample performed in H = 5 T and T = 10 K. Insets: difference of measured spectra relative to a Co^{2+} reference spectrum. Co^{2+} data were taken from ref 53. (b) Anomalous Hall resistance versus magnetic field with increasing dose, as labeled, with the temperature fixed at 2 K and the magnetic field orientated out-of-plane for all panels and also in-plane for the highest dose (9 × 10^{14} cm^{-2}, right). Inset shows the difference between the anomalous Hall resistance taken on the up-sweep and down-sweep, $\Delta R_{xy,A}$.

TRIM.SP for muons[50,51] in comparison to the helium-dosed profile calculated with SRIM.[52] The MVF is found to turn on below 150 K, as marked by the dashed gray line, and steadily grows as the temperature is reduced. In addition to the high-temperature turn-on, there is a transition at 25 K with an upturn in the MVF also marked by a dashed gray line. The MVF peaks at around 55%, which is expected for the inhomogeneous profiles of both the helium and the muons, which probe simultaneously optimally and underdosed regions of the film, as discussed later for the anomalous Hall effect. Moreover, in pristine films there is a weak magnetic signature, which likely originates from native oxygen vacancies on the surface,[33] as discussed below. The key here is that there is a strong magnetic signature in the bulk of the film. This shows that the distortions produced by the helium cause bulk magnetism. This effect cannot be associated with native oxygen vacancies because it is significantly higher in MVF than the pristine films. Altogether, muon spectroscopy conclusively demonstrates that the helium implantation process can be used to induce stable bulk magnetism in otherwise nonmagnetic $PdCoO_2$.

This emergent magnetism is further interrogated using X-ray magnetic circular dichroism (XMCD) to observe element-specific charge and spin state evolutions with ion implantation. Figure 3a shows the XMCD signal for a pristine sample (top) and a sample dosed into the ferromagnetic regime (6 × 10^{14} cm^{-2}, bottom) versus photon energy as solid blue curves, which were performed at the Co L_3 edge in a magnetic field of ±5 T and a temperature of 10 K. First, the pristine sample shows a clear nonzero XMCD signal, indicating the presence of moments on the Co site. There is an excellent agreement between the reference spectrum for Co^{2+} (shown in gray; from ref 53) and the pristine sample (shown in blue), which indicates percent-level oxygen vacancies. This can be seen more clearly in the inset, where the reference spectrum was subtracted from the pristine $PdCoO_2$ spectrum. This is consistent with oxygen vacancies being the origin for the nonzero MVF shown for the pristine film in Figure 2c. In contrast, the implanted sample shows a larger (≈2−3×) XMCD signal with a significantly different line shape, which can be seen by comparison with the same Co^{2+} reference in the main panel and inset. The change in line shape indicates a clear deviation from Co^{2+}, which is consistent with a modification of the Co^{3+} spin state.[54] This shows that the magnetic state induced with implantation is different than the magnetic character of oxygen vacancies related to magnetic Co^{2+}, which is confirmed next by contrasting the dramatic difference in Hall response for pristine vs 6 × 10^{14} cm^{-2}. Based on the percent level of magnetic Co via XMCD, the length scale of the magnetic interaction must be on the order of nanometers near the paramagnetic−ferromagnetic crossover. This is consistent with the magnetic interaction being long range in nature and mediated by the itinerate electrons in the Pd layer via, for example, the RKKY mechanism,[55] which are dominated by the itinerate Pd states.

The AHE is an extremely sensitive indicator of a material's underlying magnetic and electronic properties, as it stems from both the internal magnetization and the properties of the conduction electrons (i.e., band structure and scattering processes; see ref 56 and Supporting Information Section III). In Figure 3b, we show the anomalous Hall resistance, $R_{xy,A}$, versus magnetic field at a temperature of 2 K for an implantation series with increasing dose, as labeled. For the pristine sample, $R_{xy,A}$ is nominally flat with a magnetic field, which indicates that there is very little magnetic response. This is consistent with nonmagnetic $PdCoO_2$, with the small background likely due to the dilute Co moments seen in XMCD (seen also in ref 30). With a small dosage, 1 × 10^{14}−2 × 10^{14} cm^{-2}, $R_{xy,A}$ becomes dramatically nonzero, indicating the emergence of magnetism. The character of the AHE is significantly different for 1 × 10^{14} cm^{-2} compared to the pristine sample, demonstrating a minor role of native oxygen vacancies. Here, $R_{xy,A}$ shows an S-shape with $R_{xy,A}(H = -9\ T) < 0$ and $R_{xy,A}(H = 9\ T) > 0$. For the low dosage, no hysteresis is observed down to 40 mK (see Figure S11), which shows that net moments have been created yet do not order; i.e., the material consists of a dynamic, disordered spin system. For 3 × 10^{14} cm^{-2}, the shape of $R_{xy,A}$ vs H is slightly flatter, and there is

https://doi.org/10.1021/acs.nanolett.3c01065
Nano Lett. XXXX, XXX, XXX−XXX

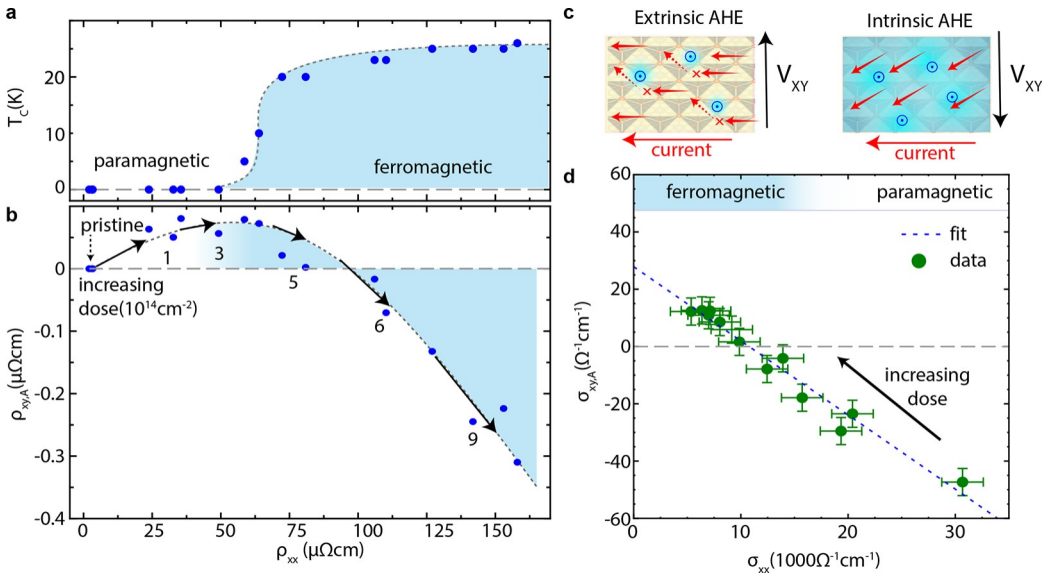

Figure 4. Tailored evolution of competing anomalous Hall effect mechanisms. (a) Ferromagnetic transition temperature versus the increase in the in-plane resistance. T_C was obtained from the data in Figure 3 at which the hysteresis vanishes. (b) Anomalous Hall resistance taken at H = 9 T plotted versus in-plane resistance where select dosages are indicated in the panel. (c) Schematic of the possible mechanisms that contribute to the anomalous Hall resistance when a current is applied toward the left in a magnetic field oriented out of the page. (left) Extrinsic scattering process off magnetic sites (blue dotted circles) in a paramagnet (net yellow background) causes deflection orthogonal to the direction of the applied current (dashed arrows). (right) Intrinsic mechanism results in a nonzero velocity of carriers orthogonal to the direction of the applied current in a ferromagnet (net blue background). Though the sign may vary, both processes cause an accumulation of charge on one side (top or bottom) of the material, resulting in a nonzero Hall voltage (V_{xy}). (d) Anomalous Hall data in (b) replotted in terms of conductivities. This follows a clear linear trend, and the corresponding fit is indicated as the dashed blue curve.

discernible hysteresis at zero magnetic field (inset of Figure 3b), which vanishes at a Curie temperature of $T_C \approx 5 \pm 2$ K. The hysteresis indicates ferromagnetic ordering, consistent with muon spectroscopy results shown in Figure 2c. At 5 × 10^{14} cm^{-2} the shape of $R_{xy,A}$ flattens, and the zero field hysteresis becomes more prominent. For dosages of 6 × 10^{14}–9 × 10^{14} cm^{-2}, $R_{xy,A}$(9 T) surprisingly shows a complete reversal of sign and grows in magnitude with hysteresis closing at a maximal T_C of around 25 ± 2 K. Moreover, the saturation field is systematically pushed to >9 T. Finally, for 9 × 10^{14} cm^{-2}, this measurement was extended to in-plane fields in which case it shows a nearly flat AHE. The pronounced difference between in-plane and out-of-plane fields indicates that the emergent ferromagnetic state likely exhibits perpendicular magnetic anisotropy with the easy axis pointed out-of-plane. Because the film is thin (10 nm), shape anisotropy should favor an in-plane easy axis, which is quite surprising and is of considerable technological relevance,[1] for example, for spin logic and memory technologies based on spin-transfer torques.[57]

The complete data set characterizing the magnetic evolution with helium-implantation-induced strain is shown in Figure 4, where T_C (extracted from the onset of hysteresis) and the anomalous Hall resistivity, $\rho_{xy,A}$(9 T) = $R_{xy,A}$(9 T) ×*thickness* are plotted versus resistivity, ρ_{xx} = R_{xx}(9 T) ×*thickness*, at 2 K (it is noted that R_{xx} has a small field dependence). From this we see that dosed $PdCoO_2$ maintains an extremely low resistivity, especially when compared to typical oxides and magnetic oxides[5,6,11] (see Figure S13 for a plot of ρ_{xx} versus dose). Furthermore, the plot of T_C shows the critical dosage where ferromagnetism onsets with T_C quickly increasing from 0 to ≈25 K and then saturating. Ferromagnetic ordering exactly coincides with the lower temperature transition in the MVF as shown in Figure 2c. In Figure 4b, $\rho_{xy,A}$(9 T) is stacked vertically below T_C to highlight the evolution of the AHE as magnetic moments arise and then subsequently form long-range order. Here, in the paramagnetic state, $\rho_{xy,A}$(9 T) increases roughly linearly with an increasing resistivity. As ferromagnetism is established (>3 × 10^{14} cm^{-2}), $\rho_{xy,A}$(9 T) flattens with increasing ρ_{xx}, and then $\rho_{xy,A}$(9 T) starts to decrease slightly faster than linearly. The coincidence of the flattening of $\rho_{xy,A}$ with the onset of ferromagnetism and the subsequent change in sign of $\rho_{xy,A}$ indicates that there are two clear competing mechanisms of the AHE, which can be finely controlled with helium implantation.

AHE arises from several mechanisms defined by specific resistivity regimes.[56] For the lowest resistivity regime (ρ_{xx} < 1 μΩ·cm), the AHE is dominated by extrinsic mechanisms, for example, skew scattering (Figure 4c, left panel). For higher resistivities (1 μΩ·cm < ρ_{xx} < 100 μΩ·cm), intrinsic effects dominate the AHE. As schematically shown in Figure 4c, right panel, the Karplus–Luttinger effect occurs when carriers obtain a component of the Fermi velocity orthogonal to the current, which is linked to the band structure in the context of the Berry phase. A comparison with theory can be made by plotting the anomalous Hall conductivity $\sigma_{xy,A}$ versus longitudinal conductivity σ_{xx}. Here, theory predicts $\sigma_{xy,A} \propto \sigma_{xx}^{n}$, with n = 1 in the extrinsic regime and n = 0 in the intrinsic regime.[56] The plot of $\sigma_{xy,A}$ versus σ_{xx} is shown in Figure 4d. The data show a very clear linear scaling (n = 1). If the anomalous contributions to the anomalous Hall conductivity are additive, then $\sigma_{xy,A} = \sigma_{xx,I} + \sigma_{xx,E}$. Here, $\sigma_{xx,I}$ is the intrinsic contribution, independent of σ_{xx}, and $\sigma_{xx,E}$ is the extrinsic contribution, linearly dependent on σ_{xx} (i.e., n = 1). This yields $\sigma_{xy,A} = \sigma_{xx,I} + \alpha \times \sigma_{xx}$, which was used to fit the data in Figure 4d and shows excellent agreement. The fit crosses $\sigma_{xy,A}$ = 0

https://doi.org/10.1021/acs.nanolett.3c01065
Nano Lett. XXXX, XXX, XXX−XXX

around $\sigma_{xx} = 10.7 \times 10^4\ \Omega^{-1}\ cm^{-1}$, and extrapolating to $\sigma_{xx} \rightarrow 0$ gives $\sigma_{xy,I} = 28\ \Omega^{-1}\ cm^{-1}$. In contrast to expectations,[56] we find no well-defined crossover regime, but rather that intrinsic and extrinsic effects are additive. It is quite interesting that skew scattering continues to be active deep in the low-conductivity regime. Specifically, the intrinsic AHE comes from anomalies in the band structure. Low-energy scattering processes (extrinsic effects such as skew scattering) are highly dependent on the electronic properties near the Fermi level, which may significantly change across this regime. The fact that these contributions continue to be additive may point out that extrinsic effects are not disrupted by changes to the electronic structure even deep into the intrinsic regime. This is likely related to the dilute density of magnetic sites where magnetism is mediated across long length scales due to the unique, highly itinerate Pd states. Furthermore, the extrapolation to $\sigma_{xx} \rightarrow 0$ enables direct identification of the strength of both the intrinsic and extrinsic contributions. The anomalous Hall conductivity in implanted $PdCoO_2$ is lower than typical magnetic metals, Fe, Co, Ni, Gd, Fe−Co/Si alloys, Mn_3Sn, Mn_3Ge, MnGe, $Co_3Sn_2S_2$, KV_3Sb_5, and Fe_3Sn_2, and oxides, $SrRuO_3$ and $(La,Sr)CoO_3$, where $\sigma_{xy,A} \approx 100–1000\ \Omega^{-1}\ cm^{-1}$ (see refs 56, 58, and 59 and references therein). Given the dilute density of magnetic sites in implanted $PdCoO_2$ based on XMCD, $\sigma_{xy,I} \approx 28\ \Omega^{-1}\ cm^{-1}$ is extremely large per magnetic site, which may result from the 2D nature and the strong spin−orbit coupling in the Pd layer. The ability to use helium to continuously tune magnetism across these regimes provides new insight into the fundamental mechanisms and gives a route to control and design a material with a desired response.

The strong hybridization among magnetic Co sites and subsequent polarization of the strong spin−orbit coupled Pd layer are central to the large, tailorable magnetic response observed. Yet, the simple distortion-induced picture regarding the CoO layer and the interplay with the itinerate Pd states that formed our hypothesis is likely an oversimplification, and many theoretical and experimental questions arise regarding the origins of the emergent magnetism. This diversity and richness of the implantation process offer many routes to design magnetism for specific applications. Gaining this control requires a deeper understanding of how the implantation process can be used to target specific defect types. Given that the magnetic ordering onset is observed at 150 K, exploring the detailed magnetic properties of each type of defect and how to target them is an important critical future question to boost T_C toward room temperature. Moreover, the use of helium to dynamically induce magnetism can be applicable beyond just $PdCoO_2$ and should be generally usable to tailor magnetism in the other Pd/Pt-based delafossites,[12] at magnetic oxide interfaces with Pd/Pt, and 2D layered magnetic materials.[60]

In contrast to adjusting preexisting magnetic properties of metals with nanometer scale resolution using ion technologies[46,47,61] or micrometer scale resolution via thermal induced optical pulses,[45] the key novelty is that it is possible to induce emergent and stable ferromagnetism in the otherwise nonmagnetic oxide material using helium implantation. This generally applicable approach solves a critical challenge for the design of magnetic responses in materials with strong spin−orbit coupling and high conductivities. Here, the magnetism is quite stable, which enables devices to be written and then erased with a high-temperature anneal. Therefore, there are many possible routes for the creation of magnetic devices by precisely controlling the implantation profile across the depth but also with nanometer-scale lateral resolution.[47] Specifically, varying the implantation dose across the thickness can enable the creation of a vertically stacked multilayer magnetic device where each layer has a specific magnetic property, laterally structured magnonic crystals, or arrays of technologies where high-conductivity, low-dissipation interconnects can be based on pristine $PdCoO_2$. As this is a fully tunable magnetic system, helium-implanted $PdCoO_2$ is a new platform to explore the interplay among local/itinerate and extrinsic/intrinsic effects that will have a profound impact on the fundamental understanding of magnetic responses and open many routes for technological adaptation.

ASSOCIATED CONTENT

Data Availability Statement

The Department of Energy will provide public access to these results of federally sponsored research in accordance with the DOE Public Access Plan (http://energy.gov/downloads/doe-public-access-plan). The data supporting this study's findings are available from the corresponding author upon reasonable request.

* Supporting Information

The Supporting Information is available free of charge at https://pubs.acs.org/doi/10.1021/acs.nanolett.3c01065.

Section I: ab-initio DFT and QMC supporting data; Section II: experimental methods; Section III: anomalous Hall effect; and Section IV: experimental supporting data (PDF)

AUTHOR INFORMATION

Corresponding Authors

Matthew Brahlek − *Materials Science and Technology Division, Oak Ridge National Laboratory, Oak Ridge, Tennessee 37831, United States;* orcid.org/0000-0003-2900-0648; Email: brahlekm@ornl.gov

Panchapakesan Ganesh − *Center for Nanophase Materials Sciences, Oak Ridge National Laboratory, Oak Ridge, Tennessee 37831, United States;* orcid.org/0000-0002-7170-2902; Email: ganeshp@ornl.gov

Authors

Alessandro R. Mazza − *Materials Science and Technology Division, Oak Ridge National Laboratory, Oak Ridge, Tennessee 37831, United States; Center for Integrated Nanotechnologies, Los Alamos National Laboratory, Los Alamos, New Mexico 87545, United States*

Abdulgani Annaberdiyev − *Center for Nanophase Materials Sciences, Oak Ridge National Laboratory, Oak Ridge, Tennessee 37831, United States*

Michael Chilcote − *Materials Science and Technology Division, Oak Ridge National Laboratory, Oak Ridge, Tennessee 37831, United States*

Gaurab Rimal − *Department of Physics and Astronomy, Rutgers, The State University of New Jersey, Piscataway, New Jersey 08854, United States;* orcid.org/0000-0002-7991-7772

Gábor B. Halász − *Materials Science and Technology Division, Oak Ridge National Laboratory, Oak Ridge, Tennessee 37831, United States*

https://doi.org/10.1021/acs.nanolett.3c01065
Nano Lett. XXXX, XXX, XXX−XXX

Anh Pham − *Center for Nanophase Materials Sciences, Oak Ridge National Laboratory, Oak Ridge, Tennessee 37831, United States*
Yun-Yi Pai − *Materials Science and Technology Division, Oak Ridge National Laboratory, Oak Ridge, Tennessee 37831, United States*
Jaron T. Krogel − *Materials Science and Technology Division, Oak Ridge National Laboratory, Oak Ridge, Tennessee 37831, United States;* orcid.org/0000-0002-1859-181X
Jason Lapano − *Materials Science and Technology Division, Oak Ridge National Laboratory, Oak Ridge, Tennessee 37831, United States*
Benjamin J. Lawrie − *Materials Science and Technology Division, Oak Ridge National Laboratory, Oak Ridge, Tennessee 37831, United States;* orcid.org/0000-0003-1431-066X
Gyula Eres − *Materials Science and Technology Division, Oak Ridge National Laboratory, Oak Ridge, Tennessee 37831, United States;* orcid.org/0000-0003-2690-5214
Jessica McChesney − *Advanced Photon Source, Argonne National Laboratory, Lemont, Illinois 60439, United States*
Thomas Prokscha − *Laboratory for Muon Spin Spectroscopy, Paul Scherrer Institute, CH-5232 Villigen PSI, Switzerland*
Andreas Suter − *Laboratory for Muon Spin Spectroscopy, Paul Scherrer Institute, CH-5232 Villigen PSI, Switzerland*
Seongshik Oh − *Department of Physics and Astronomy, Rutgers, The State University of New Jersey, Piscataway, New Jersey 08854, United States;* orcid.org/0000-0003-1681-516X
John W. Freeland − *Advanced Photon Source, Argonne National Laboratory, Lemont, Illinois 60439, United States*
Yue Cao − *Materials Science Division, Argonne National Laboratory, Lemont, Illinois 60439, United States*
Jason S. Gardner − *Materials Science and Technology Division, Oak Ridge National Laboratory, Oak Ridge, Tennessee 37831, United States;* orcid.org/0000-0002-7823-4072
Zaher Salman − *Laboratory for Muon Spin Spectroscopy, Paul Scherrer Institute, CH-5232 Villigen PSI, Switzerland*
Robert G. Moore − *Materials Science and Technology Division, Oak Ridge National Laboratory, Oak Ridge, Tennessee 37831, United States;* orcid.org/0000-0002-1608-5411
T. Zac Ward − *Materials Science and Technology Division, Oak Ridge National Laboratory, Oak Ridge, Tennessee 37831, United States;* orcid.org/0000-0002-1027-9186
Complete contact information is available at: https://pubs.acs.org/10.1021/acs.nanolett.3c01065

Author Contributions

M.B., A.R.M., and T.Z.W. conceived the project; A.A., A.P., J.T.K., and P.G. performed the theoretical calculations, as directed by P.G.; M.B., A.R.M., and M.C. performed the implantation under the direction of T.Z.W.; G.R. and S.O. performed the synthesis in coordination with M.B.; M.B., M.C., and G.E. performed the structural characterization; J.W.F. performed the XMCD; M.B. performed the transport measurements with help from J.L. and Y.-Y.P., with input from G.H.; R.G.M. performed the spectroscopy with assistance from Y.C. and J.M.; Z.S., M.B., T.Z.W., and J.S.G. performed muon spin rotations with assistance from T.P. and A.S.; M.B. wrote the manuscript with input from all coauthors and directed the work.

Notes

The authors declare no competing financial interest.

ACKNOWLEDGMENTS

Processing, electronic characterization and manuscript were supported by the U.S. Department of Energy (DOE), Office of Science, Basic Energy Sciences (BES), Materials Sciences and Engineering Division. Spectroscopy was supported by the U.S. Department of Energy, Office of Science, National Quantum Information Science Research Centers, Quantum Science Center. Part of the theory work (quantum Monte Carlo and density functional theory using Quantum ESPRESSO) has been supported by the U.S. Department of Energy, Office of Science, Basic Energy Sciences, Materials Sciences and Engineering Division, as part of the Computational Materials Sciences Program and Center for Predictive Simulation of Functional Materials. Initial theory screening (density functional theory using VASP) that formed the basis of current theory-work was supported by the Center for Nanophase Materials Sciences (CNMS), which is a U.S. Department of Energy, Office of Science User Facility at Oak Ridge National Laboratory. An award of computer time was provided by the Innovative and Novel Computational Impact on Theory and Experiment (INCITE) program. Part of this research (quantum Monte Carlo) used resources of the Oak Ridge Leadership Computing Facility, which is a DOE Office of Science User Facility supported under Contract No. DE-AC05-00OR22725. Part of this research (quantum Monte Carlo) used resources of the Argonne Leadership Computing Facility, which is a DOE Office of Science User Facility supported under Contract No. DE-AC02-06CH11357. Part of this research (density functional theory) used resources of the National Energy Research Scientific Computing Center (NERSC), a U.S. Department of Energy Office of Science User Facility located at Lawrence Berkeley National Laboratory, operated under Contract No. DE-AC02-05CH11231. This paper describes objective technical results and analysis. Any subjective views or opinions that might be expressed in the paper do not necessarily represent the views of the U.S. Department of Energy or the United States Government. The use of the Advanced Photon Source, Argonne National Laboratory was supported by the U.S. Department of Energy, Office of Science, Basic Energy Sciences, under Contract No. DE-AC02-06CH11357. The use of the Swiss Muon Source (SμS) and Swiss Light Source (SLS), Paul Scherrer Institute, Villigen, Switzerland. Muon spectroscopy was partially supported by Laboratory Directed Research and Development Program of Oak Ridge National Laboratory, managed by UT-Battelle, LLC, for the U.S. Department of Energy. Synthesis was supported by National Science Foundation (NSF) Grant No. DMR2004125 and Army Research Office (ARO) Grant No. W911NF2010108. Work at CINT, an Office of Science User Facility operated for the U.S. Department of Energy Office of Science through the Los Alamos National Laboratory. Los Alamos National Laboratory is operated by Triad National Security, LLC, for the National Nuclear Security Administration of U.S. Department of Energy (Contract No. 89233218CNA000001).

https://doi.org/10.1021/acs.nanolett.3c01065
Nano Lett. XXXX, XXX, XXX−XXX

REFERENCES

(1) Hellman, F.; Hoffmann, A.; Tserkovnyak, Y.; Beach, G. S. D.; Fullerton, E. E.; Leighton, C.; MacDonald, A. H.; Ralph, D. C.; Arena, D. A.; Durr, H. A.; Fischer, P.; Grollier, J.; Heremans, J. P.; Jungwirth, T.; Kimel, A. v.; Koopmans, B.; Krivorotov, I. N.; May, S. J.; Petford-Long, A. K.; Rondinelli, J. M.; Samarth, N.; Schuller, I. K.; Slavin, A. N.; Stiles, M. D.; Tchernyshyov, O.; Thiaville, A.; Zink, B. L. Interface-induced phenomena in magnetism. *Rev. Mod. Phys.* 2017, *89*, 025006.

(2) Gushi, F.; Lee, J. H.; Trier, F.; Bibes, M.; Winter, S. M; Valenti, R.; Son, Y.-W.; Taillefer, L.; Heil, C.; Figueroa, A. I.; Placais, B.; Wu, Q.; Yazyev, O. V.; Bakkers, E. P. A. M.; Nygard, J.; Forn-Diaz, P.; De Franceschi, S.; McIver, J. W.; Torres, L. E. F. F.; Low, T.; Kumar, A.; Galceran, R.; Valenzuela, S. O.; Costache, M. V.; Manchon, A.; Kim, E.-A.; Schleder, G. R.; Fazzio, A.; Roche, S. The 2021 quantum materials roadmap. *Journal of Physics: Materials.* 2020, *3*, 042006.

(3) Hirohata, A.; Yamada, K.; Nakatani, Y.; Prejbeanu, I.-L.; Diény, B.; Pirro, P.; Hillebrands, B. Review on spintronics: Principles and device applications. *J. Magn. Magn. Mater.* 2020, *509*, 166711.

(4) Matsukura, F.; Tokura, Y.; Ohno, H. Control of magnetism by electric fields. *Nat. Nanotechnol.* 2015, *10*, 209−220.

(5) Chen, X.; Wu, Q.; Zhang, L.; Hao, Y.; Han, M.-G.; Zhu, Y.; Hong, X. Anomalous Hall effect and perpendicular magnetic anisotropy in ultrathin ferrimagnetic $NiCo_2O_4$ films. *Appl. Phys. Lett.* 2022, *120*, 242401.

(6) Xia, J.; Siemons, W.; Koster, G.; Beasley, M. R.; Kapitulnik, A. Critical thickness for itinerant ferromagnetism in ultrathin films of SrRuO3. *Phys. Rev. B* 2009, *79*, 140407.

(7) Rastogi, A.; Brahlek, M.; Ok, J. M.; Liao, Z.; Sohn, C.; Feldman, S.; Lee, H. N. Metal-insulator transition in (111) SrRuO3 ultrathin films. *APL Mater.* 2019, 7.

(8) Du, D.; Manzo, S.; Zhang, C.; Saraswat, V.; Genser, K. T.; Rabe, K. M.; Voyles, P. M.; Arnold, M. S.; Kawasaki, J. K. Epitaxy, exfoliation, and strain-induced magnetism in rippled Heusler membranes. *Nat. Commun.* 2021, *12*, 2494.

(9) Bhattacharya, A.; May, S. J. Magnetic Oxide Heterostructures. *Annu. Rev. Mater. Res.* 2014, *44*, 65−90.

(10) Moyer, J. A.; Eaton, C.; Engel-Herbert, R. Highly Conductive SrVO3 as a bottom electrode for functional perovskite oxides. *Adv. Mater.* 2013, *25*, 3578−82.

(11) Zhang, L.; Zhou, Y.; Guo, L.; Zhao, W.; Barnes, A.; Zhang, H.-T.; Eaton, C.; Zheng, Y.; Brahlek, M.; Haneef, H. F.; Podraza, N. J.; Chan, M. H. W.; Gopalan, V.; Rabe, K. M.; Engel-Herbert, R. Correlated metals as transparent conductors. *Nat. Mater.* 2016, *15*, 204−210.

(12) Mackenzie, A. P. The properties of ultrapure delafossite metals. *Rep. Prog. Phys.* 2017, *80*, 032501.

(13) Harada, T.; Okada, Y. Metallic delafossite thin films for unique device applications. *APL Mater.* 2022, *10*, 070902.

(14) Takatsu, H.; Ishikawa, J. J.; Yonezawa, S.; Yoshino, H.; Shishidou, T.; Oguchi, T.; Murata, K.; Maeno, Y. Extremely Large Magnetoresistance in the Nonmagnetic Metal PdCoO2. *Phys. Rev. Lett.* 2013, *111*, 056601.

(15) Moll, P. J. W.; Kushwaha, P.; Nandi, N.; Schmidt, B.; Mackenzie, A. P. Evidence for hydrodynamic electron flow in $PdCoO_2$. *Science.* 2016, *351*, 1061−4.

(16) Bachmann, M. D.; Sharpe, A. L.; Baker, G.; Barnard, A. W.; Putzke, C.; Scaffidi, T.; Nandi, N.; McGuinness, P. H.; Zhakina, E.; Moravec, M.; Khim, S.; König, M.; Goldhaber-Gordon, D.; Bonn, D. Mackenzie, A. P.; Moll, P. J. W. Directional ballistic transport in dimensional metal PdCoO2. *Nature Physics 2022 18:7.* 2022, PdCoO2. *npj Quantum Mater.* 2022, *7*, 1−6.

(17) Putzke, C.; Bachmann, M. D.; McGuinness, P.; Zhakina, E.; Sunko, V.; Konczykowski, M.; Oka, T.; Moessner, R.; Stern, A.; M.; Khim, S.; Mackenzie, A. P.; Moll, P. J. W. h/e oscillations transport of delafossites. *Science (1979).* 2020, *368*, *2*, 013282.

(18) Harada, T.; Tsukazaki, A. Control of Schottky barrier height in metal/β-Ga2O3 junctions by insertion of PdCoO2 layers. *APL Mater.* 2020, *8*, 041109.

(19) Rimal, G.; Schmidt, C.; Hijazi, H.; Feldman, L. C.; Liu, Y.; Skoropata, E.; Lapano, J.; Brahlek, M.; Mukherjee, D.; Unocic, R. R.; Chisholm, M. F.; Sun, Y.; Yu, H.; Ramanathan, S.; Sun, C.-J.; Zhou, H.; Oh, S. Effective reduction of PdCoO2 thin films via hydrogenation and sign tunable anomalous Hall effect. *Phys. Rev. Mater.* 2021, *5*, L052001.

(20) Liu, Y.; Rimal, G.; Narasimhan, P.; Oh, S. Anomalous Hall effect in electrolytically reduced PdCoO2 thin films. *Thin Solid Films.* 2022, *751*, 139197.

(21) Podjaski, F.; Weber, D.; Zhang, S.; Diehl, L.; Eger, R.; Duppel, V.; Alarcón-Lladó, E.; Richter, G.; Haase, F.; Fontcuberta i Morral, A.; Scheu, C.; Lotsch, B. v. Rational strain engineering in delafossite oxides for highly efficient hydrogen evolution catalysis in acidic media. *Nat. Catal.* 2020, *3*, 55−63.

(22) Sunko, V.; Mcguinness, P. H.; Chang, C. S.; Zhakina, E.; Khim, S.; Dreyer, C. E.; Konczykowski, M.; Borrmann, H.; Moll, P. J. W.; König, M.; Muller, D. A.; Mackenzie, A. P. Controlled Introduction of Defects to Delafossite Metals by Electron Irradiation. *Phys. Rev. X.* 2020, *10*, 021018.

(23) Lu, Q.; Martins, H.; Kahk, J. M.; Rimal, G.; Oh, S.; Vishik, I.; Brahlek, M.; Chueh, W. C.; Lischner, J.; Nemsak, S. Layer-resolved many-electron interactions in delafossite PdCoO2 from standing-wave photoemission spectroscopy. *Commun. Phys.* 2021, *4*, 1−8.

(24) Ong, K. P.; Zhang, J.; Tse, J. S.; Wu, P. Origin of anisotropy and metallic behavior in delafossite PdCoO2. *Phys. Rev. B* 2010, *81*, 115120.

(25) Mekata, M.; Sugino, T.; Oohara, A.; Oohara, Y.; Yoshizawa, H. Magnetic structure of antiferromagnetic PdCrO2 possible degenerate helices on a rhombohedral lattice. *Physica B: Physics of Condensed Matter* 1995, 213−214 221−223.

(26) Goodenough, J. B. An interpretation of the magnetic properties of the perovskite-type mixed crystals La1−xSrxCoO3−λ. *Journal of Physics and Chemistry of Solids.* 1958, *6*, 287−297.

(27) Walter, J.; Hara, S.; Suzuki, M.; Suzuki, L. S. Magnetism in Palladium Experimental Results in View of Theoretic Predictions. In *Molecular Low Dimensional and Nanostructured Materials for Advanced Applications*; Graja, A., Bułka, B. R., Kajzar, F., Eds.; Springer Science +Business Media: Dordrecht, 2002; Vol. *59*, pp 329−333.

(28) Bouarab, S.; Demangeat, C.; Mokrani, A.; Dreyssé, H. Onset of magnetism in palladium slabs. *Phys. Lett. A* 1990, *151*, 103−105.

(29) Fitzsimmons, M. R.; Bader, S. D.; Borchers, J. A.; Felcher, G. P.; Furdyna, J. K.; Hoffmann, A.; Kortright, J. B.; Schuller, I. K.; Schulthess, T. C.; Sinha, S. K.; Toney, M. F.; Weller, D.; Wolf, S. Neutron scattering studies of nanomagnetism and artificially structured materials. *J. Magn. Magn. Mater.* 2004, *271*, 103−146.

(30) Song, Q.; Sun, J.; Parzyck, C. T.; Miao, L.; Xu, Q.; Hensling, F. V. E.; Barone, M. R.; Hu, C.; Kim, J.; Faeth, B. D.; Paik, H.; King, P. D. C.; Shen, K. M.; Schlom, D. G. Growth of PdCoO2 films with controlled termination by molecular-beam epitaxy and determination of their electronic structure by angle-resolved photoemission spectroscopy. *APL Mater.* 2022, *10*, 091113.

(31) Mazzola, F.; Sunko, V.; Khim, S.; Rosner, H.; Kushwaha, P.; Clark, O. J.; Bawden, L.; Markovic, I.; Kim, T. K.; Hoesch, M.; Mackenzie, A. P.; King, P. D. C. Itinerant ferromagnetism of the Pd-terminated polar surface of PdCoO2. *Proc. Natl. Acad. Sci. U. S. A.* 2018, *115*, 12956−12960.

(32) Mazzola, F.; Yim, C. M.; Sunko, V.; Khim, S.; Kushwaha, P.; Clark, O. J.; Bawden, L.; Markovic, I.; Chakraborti, D.; Kim, T. K.; A.; Hoesch, M.; Mackenzie, A. P.; Wahl, P.; King, P. D. C. Tuneable the two-electron−magnon coupling of ferromagnetic surface states in *18*, 819−824.

(33) Harada, T.; Sugawara, K.; Fujiwara, K.; Kitamura, M.; Ito, S.; Nojima, T.; Horiba, K.; Kumigashira, H.; Takahashi, T.; Sato, T.; König, Tsukazaki, A. Anomalous Hall effect at the spontaneously electron-in interlayer doped polar surface of PdCoO2 ultrathin films. *Phys. Rev. Res.* 2020, 1234−1238.

https://doi.org/10.1021/acs.nanolett.3c01065
Nano Lett. XXXX, XXX, XXX−XXX

(34) Guo, H.; Dong, S.; Rack, P.; Budai, J.; Beekman, C.; Gai, Z.; Siemons, W.; Gonzalez, C.; Timilsina, R.; Wong, A. T.; Herklotz, A.; Snijders, P. C.; Dagotto, E.; Ward, T. Z. Strain Doping: Reversible Single-Axis Control of a Complex Oxide Lattice via Helium Implantation. *Phys. Rev. Lett.* 2015, *114*, 256801.
(35) Skoropata, E.; Mazza, A. R.; Herklotz, A.; Ok, J. M.; Eres, G.; Brahlek, M.; Charlton, T. R.; Lee, H. N.; Ward, T. Z. Post-synthesis control of Berry phase driven magnetotransport in SrRuO3 films. *Phys. Rev. B* 2021, *103*, 085121.
(36) Herklotz, A.; Wong, A. T.; Meyer, T.; Biegalski, M. D.; Lee, H. N.; Ward, T. Z. Controlling Octahedral Rotations in a Perovskite via Strain Doping. *Sci. Rep.* 2016, *6*, 26491.
(37) Mazza, A. R.; Miettinen, A.; Gai, Z.; He, X.; Charlton, T. R.; Ward, T. Z.; Conrad, M.; Bian, G.; Conrad, E. H.; Miceli, P. F. The structural modification and magnetism of many-layer epitaxial graphene implanted with low-energy light ions. *Carbon N Y.* 2022, *192*, 462−472.
(38) Giannozzi, P.; Baroni, S.; Bonini, N.; Calandra, M.; Car, R.; Cavazzoni, C.; Ceresoli, D.; Chiarotti, G. L; Cococcioni, M.; Dabo, I.; Dal Corso, A.; de Gironcoli, S.; Fabris, S.; Fratesi, G.; Gebauer, R.; Gerstmann, U.; Gougoussis, C.; Kokalj, A.; Lazzeri, M.; Martin-Samos, L.; Marzari, N.; Mauri, F.; Mazzarello, R.; Paolini, S.; Pasquarello, A.; Paulatto, L.; Sbraccia, C.; Scandolo, S.; Sclauzero, G.; Seitsonen, A. P; Smogunov, A.; Umari, P.; Wentzcovitch, R. M QUANTUM ESPRESSO: a modular and open-source software project for quantum simulations of materials. *Journal of Physics: Condensed Matter.* 2009, *21*, 395502.
(39) Kim, J.; Baczewski, A. D.; Beaudet, T. D.; Benali, A.; Bennett, M. C.; Berrill, M. A.; Blunt, N. S.; Borda, E. J. L.; Casula, M.; Ceperley, D. M.; Chiesa, S.; Clark, B. K.; Clay, R. C.; Delaney, K. T.; Dewing, M.; Esler, K. P.; Hao, H.; Heinonen, O.; Kent, P. R. C.; Krogel, J. T.; Kylänpää, I.; Li, Y. W.; Lopez, M. G.; Luo, Y.; Malone, F. D.; Martin, R. M.; Mathuriya, A.; McMinis, J.; Melton, C. A.; Mitas, L.; Morales, M. A.; Neuscamman, E.; Parker, W. D.; D. Pineda Flores, S.; Romero, N. A.; Rubenstein, B. M.; Shea, J. A. R.; Shin, H.; Shulenburger, L.; Tillack, A. F.; Townsend, J. P.; Tubman, N. M.; van der Goetz, B.; Vincent, J. E.; Yang, D. C.; Yang, Y.; Zhang, S.; Zhao, L. QMCPACK : an open source ab initio quantum Monte Carlo package for the electronic structure of atoms, molecules and solids. *Journal of Physics: Condensed Matter.* 2018, *30*, 195901.
(40) Kent, P. R. C.; Annaberdiyev, A.; Benali, A.; Bennett, M. C.; Landinez Borda, E. J.; Doak, P.; Hao, H.; Jordan, K. D.; Krogel, J. T.; Kylänpää, I.; Lee, J.; Luo, Y.; Malone, F. D.; Melton, C. A.; Mitas, L.; Morales, M. A.; Neuscamman, E.; Reboredo, F. A.; Rubenstein, B.; Saritas, K.; Upadhyay, S.; Wang, G.; Zhang, S.; Zhao, L. QMCPACK: Advances in the development, efficiency, and application of auxiliary field and real-space variational and diffusion quantum Monte Carlo. *J. Chem. Phys.* 2020, *152*, 174105.
(41) Foulkes, W. M. C.; Mitas, L.; Needs, R. J.; Rajagopal, G. Quantum Monte Carlo simulations of solids. *Rev. Mod. Phys.* 2001, *73*, 33−83.
(42) Ok, J. M.; Brahlek, M.; Choi, W. S.; Roccapriore, K. M.; Chisholm, M. F.; Kim, S.; Sohn, C.; Skoropata, E.; Yoon, S.; Kim, J. S.; Lee, H. N. Pulsed-laser epitaxy of metallic delafossite PdCrO2 films. *APL Mater.* 2020, *8*, 051104.
(43) Wolff, N.; Schwaigert, T.; Siche, D.; Schlom, D. G.; Klimm, D. Growth of CuFeO2 single crystals by the optical floating-zone technique. *J. Cryst. Growth.* 2020, *532*, 125426.
(44) Brahlek, M.; Rimal, G.; Ok, J. M.; Mukherjee, D.; Mazza, A. R.; Lu, Q.; Lee, H. N.; Ward, T. Z.; Unocic, R. R.; Eres, G.; Oh, S. Growth of metallic delafossite PdCoO2 by molecular beam epitaxy. *Phys. Rev. Mater.* 2019, *3*, 093401.
(45) Mei, A. B.; Gray, I.; Tang, Y.; Schubert, J.; Werder, D.; Bartell, J.; Ralph, D. C.; Fuchs, G. D.; Schlom, D. G. Local Photothermal Control of Phase Transitions for On-Demand Room-Temperature Rewritable Magnetic Patterning. *Adv. Mater.* 2020, *32*, 2001080.
(46) Fassbender, J.; McCord, J. Magnetic patterning by means of ion irradiation and implantation. *J. Magn. Magn. Mater.* 2008, *320*, 579−596.
(47) Kim, S.; Lee, S.; Ko, J.; Son, J.; Kim, M.; Kang, S.; Hong, J. Nanoscale patterning of complex magnetic nanostructures by reduction with low-energy protons. *Nat. Nanotechnol.* 2012, *7*, 567−571.
(48) Morenzoni, E.; Gluckler, H.; Prokscha, T.; Weber, H. P.; Forgan, E. M.; Jackson, T. J.; Luetkens, H.; Niedermayer, C.; Pleines, M.; Birke, M.; Hofer, A.; Litterst, J.; Riseman, T.; Schatz, G. Low-energy μSR at PSI: present and future. *Physica B Condens Matter.* 2000, *289−290*, 653−657.
(49) Prokscha, T.; Morenzoni, E.; Deiters, K.; Foroughi, F.; George, D.; Kobler, R.; Suter, A.; Vrankovic, V. The new beam at PSI: A hybrid-type large acceptance channel for the generation of a high intensity surface-muon beam. *Nucl. Instrum Methods Phys. Res. A* 2008, *595*, 317−331.
(50) Morenzoni, E.; Gluckler, H.; Prokscha, T.; Khasanov, R.; Luetkens, H.; Birke, M.; Forgan, E. M.; Niedermayer, Ch.; Pleines, M. Implantation studies of keV positive muons in thin metallic layers. *Nucl. Instrum Methods Phys. Res. B* 2002, *192*, 254−266.
(51) Eckstein, W. *Computer Simulation of Ion-Solid Interactions*; Springer: Berlin, 1991; Vol. *10*.
(52) Ziegler, J. F.; Ziegler, M. D.; Biersack, J. P. SRIM − The stopping and range of ions in matter (2010). *Nucl. Instrum Methods Phys. Res. B* 2010, *268*, 1818−1823.
(53) Morrow, R.; Samanta, K.; Saha Dasgupta, T.; Xiong, J.; Freeland, J. W.; Haskel, D.; Woodward, P. M. Magnetism in Ca2CoOsO6 and Ca2NiOsO6: Unraveling the Mystery of Super-exchange Interactions between 3d and 5d Ions. *Chem. Mater.* 2016, *28*, 3666−3675.
(54) Haverkort, M. W.; Hu, Z.; Cezar, J. C.; Burnus, T.; Hartmann, H.; Reuther, M.; Zobel, C.; Lorenz, T.; Tanaka, A.; Brookes, N. B.; Hsieh, H. H.; Lin, H.-J.; Chen, C. T.; Tjeng, L. H. Spin State Transition in LaCoO3 Studied Using Soft X-ray Absorption Spectroscopy and Magnetic Circular Dichroism. *Phys. Rev. Lett.* 2006, *97*, 176405.
(55) Crangle, J.; Scott, W. R. Dilute Ferromagnetic Alloys. *J. Appl. Phys.* 1965, *36*, 921.
(56) Nagaosa, N.; Sinova, J.; Onoda, S.; MacDonald, A. H.; Ong, N. P. Anomalous Hall effect. *Rev. Mod. Phys.* 2010, *82*, 1539−1592.
(57) Ikeda, S.; Miura, K.; Yamamoto, H.; Mizunuma, K.; Gan, H. D.; Endo, M.; Kanai, S.; Hayakawa, J.; Matsukura, F.; Ohno, H. A perpendicular-anisotropy CoFeB−MgO magnetic tunnel junction. *Nat. Mater.* 2010, *9*, 721−724.
(58) Fujishiro, Y.; Kanazawa, N.; Kurihara, R.; Ishizuka, H.; Hori, T.; Yasin, F. S.; Yu, X.; Tsukazaki, A.; Ichikawa, M.; Kawasaki, M.; Nagaosa, N.; Tokunaga, M.; Tokura, Y. Giant anomalous Hall effect from spin-chirality scattering in a chiral magnet. *Nat. Commun.* 2021, *12*, 317.
(59) Yang, S.-Y.; Wang, Y.; Ortiz, B. R.; Liu, D.; Gayles, J.; Derunova, E.; Gonzalez-Hernandez, R.; Smejkal, L.; Chen, Y.; Parkin, S. S. P.; Wilson, S. D.; Toberer, E. S.; McQueen, T.; Ali, M. N. Giant, unconventional anomalous Hall effect in the metallic frustrated magnet candidate, KV3Sb5. *Sci. Adv.* 2020, *6*, 6.
(60) Mak, K. F.; Shan, J.; Ralph, D. C. Probing and controlling magnetic states in 2D layered magnetic materials. *Nature Reviews Physics.* 2019, *1*, 646−661.
(61) Bali, R.; Wintz, S.; Meutzner, F.; Hubner, R.; Boucher, R.; Unal, A. A.; Valencia, S.; Neudert, A.; Potzger, K.; Bauch, J.; Kronast, F.; Facsko, S.; Lindner, J.; Fassbender, J. Printing Nearly-Discrete Magnetic Patterns Using Chemical Disorder Induced Ferromagnetism. *Nano Lett.* 2014, *14*, 435−441.

https://doi.org/10.1021/acs.nanolett.3c01065
Nano Lett. XXXX, XXX, XXX−XXX